PROCEEDINGS OF SCIENCE

Enhanced durability NEA surface layer for GaAs photocathodes using Cs, O_2, and Li[†]

Maximilian Herbert,[a,*] **Joachim Enders,**[a] **Markus Engart,**[a] **Maximilian Meier,**[a] **Julian Schulze,**[a] **Vincent Wende**[a] **and Victor Winter**[a]

[a] *Institut für Kernphysik, Fachbereich Physik, Technische Universität Darmstadt, Schlossgartenstr. 9, 64289 Darmstadt, Germany*

E-mail: mherbert@ikp.tu-darmstadt.de

Photocathodes based on GaAs are used in photo-electron sources to supply spin-polarized, high-current electron beams for accelerator applications. A thin surface layer, typically comprised of Cs and an oxidant, needs to be applied to such photocathodes during an activation process in order to achieve negative electron affinity (NEA). The NEA layer and the associated quantum efficiency (QE) deteriorates over time. This decay is characterized by the so-called lifetime, a crucial parameter for photo-electron source operation. An increase of surface-layer durability and, hence, lifetime by adding Li during activation has been successfully shown in previous studies. Results of recent lifetime studies of bulk GaAs photocathodes activated with Cs, O_2, and Li using the activation chamber of the Photo-CATCH setup at Technische Universität Darmstadt will be presented, as well as additional measurements planned in the future.

20th Workshop on Polarized Sources, Targets and Polarimetry (PSTP2024),
22-27 September, 2024
Newport News, VA, United States of America

[†]Work supported by DFG (GRK 2128 "AccelencE", project number 264883531)
[*]Speaker

 ISSN 1824-8039 . Published by SISSA Medialab.

PoS(PSTP2024)055

1. Introduction

State-of-the-art particle accelerator applications such as energy-recovery linacs (ERLs [1–4]), positron sources [5, 6] and colliders [7–9] demand high-current electron beams with a high degree of spin-polarization. Operating a direct-current (DC) high-voltage (HV) photo-emission gun using negative electron affinity (NEA) photocathodes based on the III-V semiconductor gallium arsenide (GaAs) has been well-established as a source of spin-polarized electron beams [10]. The NEA surface layer, however, is very sensitive and deteriorates over time. Hence, an optimization of the electron yield as well as maximizing the extracted charge is required when serving demanding applications like those mentioned above.

In order to faciliate research and development studies on GaAs-based NEA photocathodes, a separate dedicated test stand for Photo-Cathode Activation, Testing, and Cleaning using atomic Hydrogen (Photo-CATCH) has been set up [11, 12] at the Institute for Nuclear Physics (IKP) of the Technische Universität Darmstadt [13], featuring a chamber for photocathode activation, as well as a -60 kV DC photo-gun with adjacent diagnostics beamline. Recent research at Photo-CATCH has focused on enhancing the surface layer and optimizing the activation process [14–18].

2. NEA surface layer for GaAs photocathodes

2.1 Activation process

In order to emit spin-polarized electrons, a GaAs photocathode must be excited with a photon energy in the range of $1.42\,\mathrm{eV} \leq E_\gamma \leq 1.76\,\mathrm{eV}$, corresponding to a wavelength in the range of $705\,\mathrm{nm} \leq \lambda \leq 873\,\mathrm{nm}$ [18]. However, the photoelectric threshold of GaAs is 5.52 eV, corresponding to a wavelength of 225 nm [19]. Therefore it must be reduced to enable spin-polarized electron emission. This can be done by adsorbing a thin layer of Cs in combination with an oxidant, typically O_2 or NF_3, onto the GaAs surface, effectively creating an NEA condition by lowering the energy level required for electron emission below the conduction band minimum, hence creating an NEA photocathode [19].

The process of adsorbing the NEA surface layer onto the photocathode is called activation, the ingredients required to form the surface are called activation agents. It requires an UHV environment with a base pressure below 10^{-10} mbar, as well as a chemically clean surface, with the latter usually provided by heat-cleaning the sample prior to the process. Then the activation agents are introduced into the chamber in a pre-defined procedure. For the measurements presented in this work, we used procedures based on the co-deposition (Co-De) procedure, as first described in [20]. The final quality of the adsorbed NEA layer after completing the activation process is characterized by the quantum efficiency η of the photocathode, defined as [21]

$$\eta(\lambda) = \frac{hc}{e} \cdot \frac{J_\mathrm{e}}{\mathcal{I}_\gamma \cdot \lambda} \approx 123.98\,\mathrm{nm\,mW\,\%\,\mu A^{-1}} \cdot \frac{I}{\lambda \cdot P_\gamma} \quad , \tag{1}$$

with the current density J_e and current I of the emitted electrons, as well as the intensity $\mathcal{I}_\gamma$, wavelength λ and power P_γ of the incident photons.

2.2 Surface layer lifetime

Due to environmental effects such as residual-gas desorption [22] and ion back-bombardment (IBB) [23], the quantum efficiency changes over time, typically displaying a decline in the form of a single-exponential decay [24]

$$\eta(t) \approx \eta(0) \cdot e^{-\frac{t}{\tau}} \quad , \tag{2}$$

characterized by the lifetime τ. Once a low threshold of η is reached, the photocathode cannot be operated further and requires cleaning and re-activation.

Another important parameter for photocathode operation in an accelerator is the extracted charge

$$Q(t) = \int_{t=0}^{t} I(\tilde{t})\mathrm{d}\tilde{t} = \frac{\lambda e}{hc} \cdot \int_{t=0}^{t} \eta(\tilde{t}) \cdot P_\gamma(\tilde{t})\mathrm{d}\tilde{t} \quad , \tag{3}$$

with $\lambda(t) \approx$ const.. A common benchmark to compare cathode performance is the charge extracted during the period τ, furthermore referred to as lifetime charge $Q(\tau)$. To obtain this value from Eq. (3), one can consider two distinct cases

$$Q(t) = \begin{cases} I_0 \cdot t & \text{for} \quad I(t) = I_0 \\ I_0 \cdot \tau \cdot \left(1 - e^{-\frac{t}{\tau}}\right) & \text{for} \quad P_\gamma(t) = P_{\gamma,0} \end{cases} \quad , \tag{4}$$

yielding

$$Q(\tau) = \begin{cases} I_0 \cdot \tau & \text{for} \quad I(t) = I_0 \\ I_0 \cdot \tau \cdot \left(1 - \frac{1}{e}\right) \approx 0.63 \cdot I_0 \cdot \tau & \text{for} \quad P_\gamma(t) = P_{\gamma,0} \end{cases} \quad . \tag{5}$$

Extracting high electron currents from the photocathode greatly amplifies the decrement of η by additional IBB [25] and heat-induced desorption [26], thereby severely limiting the total charge that can be extracted before the photocathode requires re-activation. For this reason, prolonged high-current operation of GaAs photocathodes has proven to be very difficult to achieve [25].

2.3 Li-Enhanced NEA surface layer

Previous studies have shown that the introduction of additional agents, such as Li [27] or Sb [28], during the activation process is beneficial for the robustness of the NEA surface layer, increasing its lifetime and opening a new possible path towards high-current applications of GaAs photocathodes. The effect of adding a second alkali metal to a Cs-NF_3 activation process was first studied by Mulhollan and Bierman in 2008, testing the robustness against CO_2 exposure and finding that the Cs-NF_3-Li surface layer performed best [27]. Mulhollan further investigated Li as an enhancing agent, finding that η was moderately reduced for higher doses of Li, and that the addition of Li had negligible effects on the spin-polarization [29]. Recently, this surface layer has been jointly investigated by the electron source groups at Thomas Jefferson Lab and TUDa, testing it during operation in a HV DC photogun, yielding an increase in extracted charge [30]. Mulhollan also successfully tested Cs-O_2-Li as NEA layer, showing results similar to Cs-NF_3-Li [29]. Further studies of this layer have been conducted at Photo-CATCH [11, 14, 15, 18], yielding significant increases in lifetime and extracted charge with only a moderate reduction of quantum efficiency [18]. The measurements presented in this work are based on these previous findings.

3. Experimental setup at Photo-CATCH

All measurements described in this work where conducted in the Photo-CATCH activation chamber, where one IG pump and one NEG pump provide a base pressure as low as 1×10^{-11} mbar after bakeout. The pressure is monitored using a cold-cathode ionization gauge[1] connected to a remote-controllable multi-channel gauge controller[2]. Each photocathode sample is set into a molybdenum photocathode holder or puck, allowing transfer of the sample between chambers. Within the activation chamber, the puck is placed on a carousel assembly that allows both vertical and radial movement. Two tungsten coils are available to heat-clean the sample surface prior to activation. A ring anode, a Cs vapor dispenser, and a Li vapor dispenser are mounted on an assembly connected to an electric feedthrough. During the activation process, the photocathode is placed approximately 10 mm above the assembly. The ring anode is connected to a powersupply capable of providing a bias voltage of up to 500 V, and to an ADC to measure the photocurrent. An external reservoir, connected to the chamber through a piezoelectric leak-valve[3] that is controlled by a precision high-voltage module[4], is used to provide oxygen. Sample illumination is facilitated using either a white-light LED array[5] or a laser diode[6] that is mounted on an adjacent laser table, providing laser light with $\lambda = (785 \pm 2)$ nm that is transported to the activation chamber through a fiber optic patch cable. Remote control and data acquisition is conducted using an EPICS IOC server, with all devices required for the activation process connected to the server either using CAN bus or serial interface. The activation process is monitored using a dedicated GUI created with Control System Studio, featuring embedded Python scripts.

Recently, the activation chamber has undergone extensive maintenance during which the activation setup received major updates. Accuracy of the anode current readout was improved by replacing the previously used ADC with a high-precision module fabricated in-house. An assembly for laser-power adjustment using a combination of a zero-order half-wave plate in a motorized precision rotation mount and a polarizing beam splitter was implemented, allowing online PID control to stabilize either laser power or photocurrent for improved measurements of $Q(\tau)$, see Eqs. (4) and (5). The laser beamline positioned below the bottom window of the chamber was reconstructed to implement a piezo-electric mirror mount and a position-sensitive photodiode for feedback control, allowing for precise positioning of the laser beam as well as conducting quantum efficiency scans of the photocathode surface. However, since the chamber had to be opened during maintenance, both dispensers had to be replaced. The new dispensers, although from the same batch than the previous ones, show different response characteristics. Hence, the previously optimized parameters for the activation process required readjustment.

[1] Pfeiffer Vacuum® IKR 270 compact cold cathode gauge
[2] Pfeiffer Vacuum® TPG 366 Maxigauge
[3] Oxford Instruments PLV1000
[4] Iseg® DPSmini DPp 10 805 24 5 M_SHV
[5] Currently, 6 SMD5050 LED Chips with a total power of 0.6 W are used.
[6] Thorlabs® L785P090

4. Experimental procedures

4.1 Activation procedure

For the measurements presented in this work, a single Zn-doped p-type bulk-GaAs sample cut from a wafer[7] polished on one side with an orientation of (100) ± 0.1°, a thickness of (500 ± 25) µm, and a carrier concentration in the range of $5 \times 10^{18}\,\mathrm{cm}^{-3}$ to $5 \times 10^{19}\,\mathrm{cm}^{-3}$ was used. During the activation process, the sample was illuminated by the white-light LED array, and the ring-anode was biased at 100 V.

4.1.1 Cs-O_2 co-deposition (scheme 1)

An activation process based on the co-deposition (Co-De) scheme, as first established in [20], was used to activate the sample with Cs and O_2. First, Cs was introduced by operating the Cs dispenser at $I_{cs} = 3.8$ A. Once the observed photocurrent had reached its saturation peak and dropped to about 75 % of the maximum value[8], O_2 was introduced by setting the piezo-electric leak valve to a pre-defined operating voltage U_{ox}, hence co-depositing Cs and O_2 onto the sample surface. Once a pre-defined pressure threshold[9] was reached within the chamber, U_{ox} was continuously adjusted to keep the pressure close to this value throughout the rest of the process. During co-deposition the photocurrent rises a second time, until a saturation peak was reached. At this point, first O_2 and then, after roughly one minute, Cs exposure was stopped and the activation process was finished. Figure 1 shows anode current and pressure as a function of time for the scheme-1 activation performed during the study presented in this work.

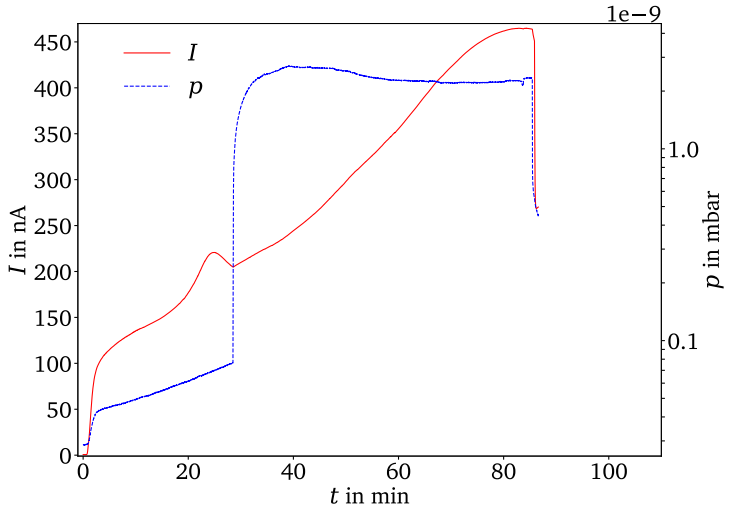

Figure 1: Anode current I and pressure p as function of time during the scheme-1 activation process, using white-light illumination. The activation yielded a final quantum efficiency of $\eta_{max} = (3.62 \pm 0.10)$ % using a 785 nm laser directly after activation.

[7] Wafer Technology Ltd.

[8] The background current from dispenser operation was subtracted from the measured anode current to obtain this value.

[9] This value was calculated from the optimal partial pressure ratio of $\frac{p_{cs}}{p_{ox}} \approx 0.043$ determined for the experimental setup during previous studies [11].

4.1.2 Cs-O_2-Li co-deposition with pulsed Li (scheme 2)

The scheme-2 activation followed the same procedure as scheme 1, but Li was introduced by operating the Li dispenser at $I_{\mathrm{li}} = 5.2\,\mathrm{A}$ during the co-deposition phase in pulses, each with a duration of 75 s and a separation of 225 s in between them, with the first pulse starting 300 s after the start of O_2 exposure. Figure 2 shows anode current and pressure as a function of time for the scheme-2 activation performed during the study presented in this work. A total of eight Li pulses were executed during this activation. Each pulse is clearly visible in both pressure and current curve.

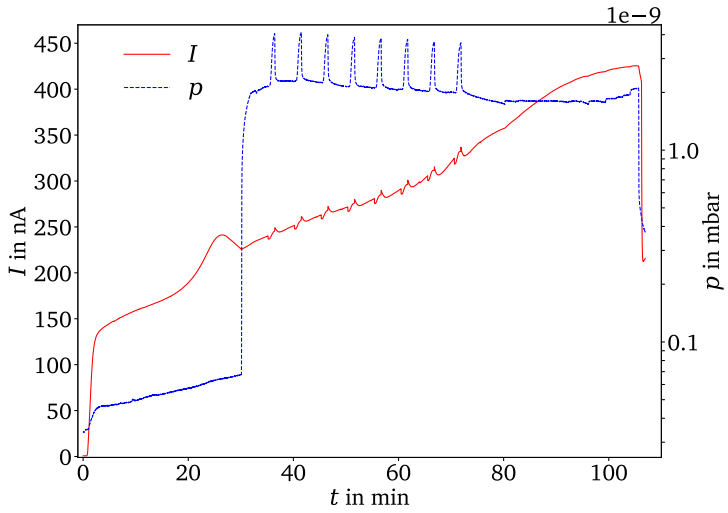

Figure 2: Anode current I and pressure p as function of time during the scheme-2 activation process, using white-light illumination. The activation yielded a final quantum efficiency of $\eta_{\mathrm{max}} = (2.69 \pm 0.07)\,\%$ causing a 785 nm laser directly after activation.

4.1.3 Cs-O_2-Li co-deposition with continuous Li (scheme 3)

The scheme-3 activation followed the same procedure as a scheme-1 process, but Li was introduced by operating the Li dispenser at $I_{\mathrm{li}} = 4.2\,\mathrm{A}$ continuously during the co-deposition phase, with Li exposure starting 300 s after the start of O_2 exposure, lasting 45 min. Figure 3 shows anode current and pressure as a function of time for the scheme-3 activation performed during the study presented in this work. The pressure increase due to Li introduction is visible as a small plateau in the pressure curve. Switching the Li dispenser on and off introduced a small indent in the current curve. An estimate of the Li dosage used in scheme 2 and scheme 3 is discussed in Section 5.1.

4.2 Quantum efficiency scan and lifetime measurement

After each activation, the sample surface was scanned with the laser spot, measuring the quantum efficiency distribution and determining the laser position that provides the maximum quantum efficiency. During the scan, the laser power was set to 50 µW. The laser spot was then set to the position of maximum quantum efficiency, and the laser power was adjusted to obtain a photocurrent of $I = 1.5\,\mu\mathrm{A}$, which was stabilized using the PID controller. After η fell below the $1/e$ threshold, the laser power was set to 50 µW, and another scan was conducted.

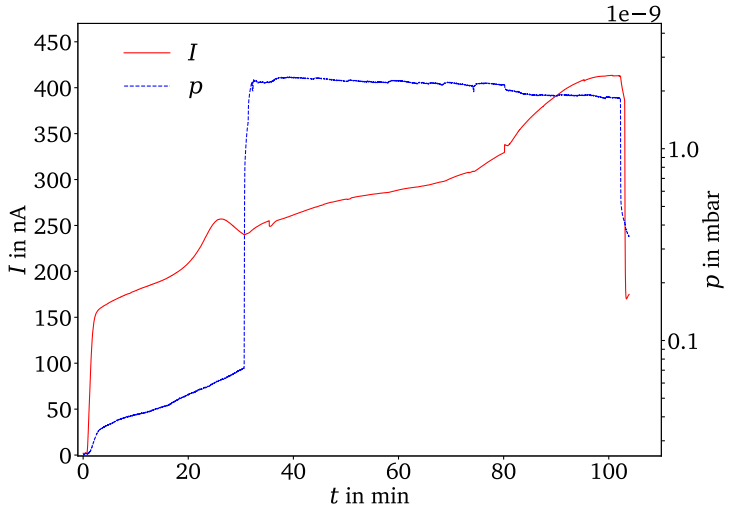

Figure 3: Anode current I and pressure p as function of time during the scheme-3 activation process, using white-light illumination. The activation yielded a final quantum efficiency of $\eta_{\text{max}} = (2.08 \pm 0.06)\,\%$ using a 785 nm laser directly after activation.

5. Results and Discussion

5.1 Activation agent dosage

The dosage of agents during each activation process was determined using the method presented in [18], with the results shown in Table 1. Several shortcomings in both experiment and evaluation result in large uncertainties:

- The dispensers are operated at a constant current. However, the applied power fluctuates during operation, thus varying the amount of introduced Cs. Since the corresponding partial pressure p_{cs} can't be monitored directly during O_2 exposure, the amount of introduced Cs must be approximated throughout most of the activation process. The same holds true for determining the Li dosage, with Li being introduced exclusively during co-deposition of Cs and O_2.

- During co-deposition, the amount of introduced O_2 must be approximated from the combined partial pressure of Cs and O_2 (and Li, in case of scheme 2 and 3). While the partial pressure of Cs is about two orders of magnitude smaller than the partial pressure of O_2, it nevertheless leads to an increased uncertainty in the determined oxygen dosage.

The resulting dosages of Cs and Li are comparable with the values obtained in [18]. After opening the chamber, we have consistently observed that higher dosage of O_2 is required to reach higher values of η. However, we have not been able to reproduce quantum efficiencies as high as previously achieved in our chamber [18]. At the time of this work, re-optimization of the activation process was not yet complete. Further measurements are required to determine the optimal dosage ratios for our setup.

Table 1: Total dosage of agents introduced over the duration of the activation process.

Scheme	Total dosages in 10^{-7} mbar s		
	D_{cs}	D_{ox}	D_{li}
1	3.3 ± 0.2	76 ± 3	-
2	3.4 ± 0.2	86 ± 3	5.1 ± 0.3
3	4.3 ± 0.5	83 ± 4	4.2 ± 0.6

5.2 Lifetime and extracted charge

Figure 4 shows the quantum efficiency, normalized to its initial value η_0 at $t = 0$, as a function of time for the different activation schemes. All measurements display a clear deviation from the expected exponential decay behavior, with η decreasing fast during the first few hours before recovering to a peak and then declining again. It is of interest to note that this initial decay is significantly stronger for both Cs-O_2-Li schemes, where η drops to about $1/e$ of its initial value after only a few hours before recovering significantly. This first minimum occurs later for the Cs-O_2 layer. Also, the relative recovery is both higher and longer for the Li-enhanced schemes, leading to a significantly higher overall lifetime and extracted charge. For scheme 3, a second run was conducted after repositioning the laser spot onto the new maximum of the surface scan following the first lifetime measurement. While η also dropped fast initially, it did not fall as low as during run 1. Also, the recovery was less pronounced, with the maximum being lower and occurring much earlier.

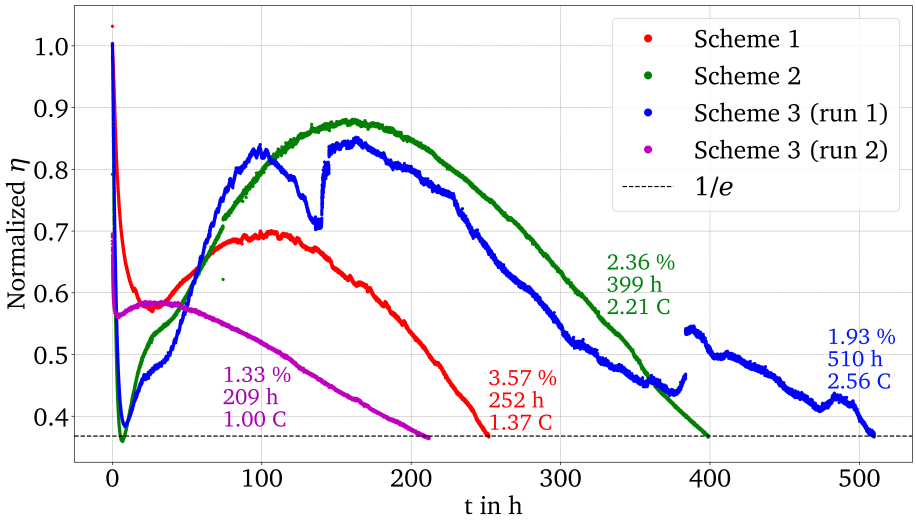

Figure 4: Quantum efficiency at 785 nm as a function of time for the different activation schemes. Each curve is labeled with initial quantum efficiency η_0, lifetime τ, and extracted charge $Q(\tau)$ in the bottom half of the figure. The data has been cut once the $1/e$ threshold was reached.

This behavior is similar to that observed in previous studies of Cs-O_2-Li at Photo-CATCH [18]. However, it is not yet clear what exactly causes this trend. As discussed in [18], interaction of residual activation agents (Cs, Li, O_2) with the surface layer is most likely. The initial fast decay may be connected with surface layer poisoning from excessive activation agents, with unstable

bonds in the surface layer disintegrating much faster than stable ones. The released activation agents then re-adsorb on the surface, forming more and more stable bonds until the surface layer has reached chemical equilibrium, leading to an increase in quantum efficiency up to a maximum. Then, damaging effects such as residual gas adsorption and IBB become dominant, resulting in the observed slow decay of quantum efficiency. Further measurements at Photo-CATCH are planned to investigate the impact of activation agent balance on the decay behavior of the quantum efficiency. The values of η_0, τ, and $Q(\tau)$ are listed in Table 2. While both Li-enhanced schemes show a significant reduction in initial quantum efficiency, they show a significant increase in both lifetime and extracted charge up to a factor of about 2 for scheme 3. For a constant current I, the condition $r_\tau \approx r_{Q(\tau)}$ should be met [18], which is not the case for the data presented here. The reason for this is that I was not constant throughout the measurements since the operational limits of the laser power-control setup proved to be insufficient. Also, the PID did not automatically re-engage once the system returned to values within its limit. Hence, the current fluctuated significantly during certain time frames of the lifetime measurements.

Table 2: Initial quantum efficiency η_0, lifetime τ, and extracted charge $Q(\tau)$, as well as the corresponding ratios of relative change compared to scheme 1. The second run for scheme 3, after repositioning the laser spot following the first lifetime measurement, was not compared directly to scheme 1. The combined lifetime and extracted charge of runs 1 and 2 for scheme 3 was compared instead.

Scheme	Run	η_0 in %	r_η	τ in h	r_τ	$Q(\tau)$ in C	$r_{Q(\tau)}$
1	1	3.57 ± 0.09	-	252 ± 1	-	1.37 ± 0.01	-
2	1	2.36 ± 0.06	0.66 ± 0.04	399 ± 1	1.58 ± 0.01	2.21 ± 0.01	1.61 ± 0.02
3	1	1.93 ± 0.05	0.54 ± 0.03	510 ± 1	2.02 ± 0.02	2.56 ± 0.01	1.87 ± 0.02
	2	1.33 ± 0.04	-	209 ± 1	-	1.00 ± 0.01	-
	1+2	-	-	719 ± 2	2.85 ± 0.02	3.56 ± 0.02	2.59 ± 0.04

Overall, the results do not match those obtained during the previous study at Photo-CATCH [18], where a lower decrease in η and a higher increase in both τ and $Q(\tau)$ was observed. There are several possible reasons:

- In the previous study, laser-spot adjustment on the sample surface had to be performed manually. Also, during the commissioning of the surface-scan setup, we discovered that the laser spot was only able to reach about 20 % of the sample surface. As will be discussed in the next section, some parts of the surface decayed significantly faster. Hence, it is possible that this influenced the results for r_η, r_τ, and $r_{Q(\tau)}$.
- Since the activation procedure has not yet been fully optimized after chamber maintenance, it is possible that the results are influenced by both the agent dosage as well as the execution of the activation procedure.
- It is not yet clear how much the addition of Li influences the severity of the initial decay. One possible cause for the steep drop could be the presence of too much Cs at the end of the activation process. If this is the case, a Cs-O_2 surface could display a decay behavior

similar to that observed for scheme 2 and scheme 3. It is therefore possible that the lifetime measurements for Cs+O_2 presented in [18] were ended prematurely, hence introducing a systematic error into the comparison with Cs-O_2-Li.

Nevertheless, the addition of Li shows a significant increase in both τ and $Q(\tau)$. The trend observed during run 1 of scheme 3 showed significant fluctuations in η. This was caused by a failure of the air conditioning unit in the laboratory about 140 h into the measurement, and a subsequent restart of the unit after about 380 h. We assume that this led to an increased fluctuation in the laser spot position on the sample surface, as will be further discussed in the following section.

5.3 Quantum efficiency scans

Figure 5 shows the surface scans for scheme 1 and scheme 2, after activation and after the lifetime measurement. Figure 6 shows the surface scans performed for scheme 3, after activation and after both run 1 and run 2. The position of the respective quantum efficiency maximum has been marked with colored circles, representing the size of the laser spot on the sample. The quantum efficiency at those positions was evaluated for all scans, as shown in Table 3, with η_1, η_2 and η_3 corresponding to the quantum efficiency value at the maximum positions of scan 1, 2, and 3, respectively. All scans have been normalized to η_1.

Table 3: Maximum quantum efficiencies η_1, η_2, and η_3 for scan 1, scan 2, and scan 3, respectively.

Scheme	Scan	t in h	η_1 in %	η_2 in %	η_3 in %
1	1	0	3.62 ± 0.10	3.00 ± 0.08	-
	2	283.5	1.05 ± 0.03	1.88 ± 0.05	-
2	1	0	2.69 ± 0.07	2.53 ± 0.07	-
	2	422.4	0.91 ± 0.02	1.72 ± 0.05	-
3	1	0	2.08 ± 0.06	1.97 ± 0.05	2.02 ± 0.05
	2	523.9	0.99 ± 0.03	1.56 ± 0.04	1.53 ± 0.04
	3	742	0.59 ± 0.02	0.80 ± 0.02	1.00 ± 0.03

The quantum-efficiency decay throughout the entire sample surface is clearly visible, with some areas decaying faster than others. The Li-enhanced surface layers resulting from scheme-2 and scheme-3 activation show significantly less relative decay of the quantum efficiency throughout the sample surface. Only the region to the lower right displayed a consistent decay, with less than 10 % of the initial value $\eta_1(t = 0)$ remaining in each scan conducted after the respective lifetime measurements.

The rate of decay can be quantified by comparing the relative change in η_1, η_2, and η_3 over the course of the lifetime measurements, see Table 4. At the position of η_1, where the laser spot was positioned during the lifetime measurements, about 30 % of the initial value remained. In comparison, for scheme 2 about 35 % and for scheme 3, about 48 % remained. At the position of η_2, where the maximum quantum efficiency was measured during the second scan, more than 60 % of the initial value remained for all three schemes. For scheme 3, the relative change at the positions of η_2 and η_3 during the first lifetime measurement was identical within the range of uncertainties, with about

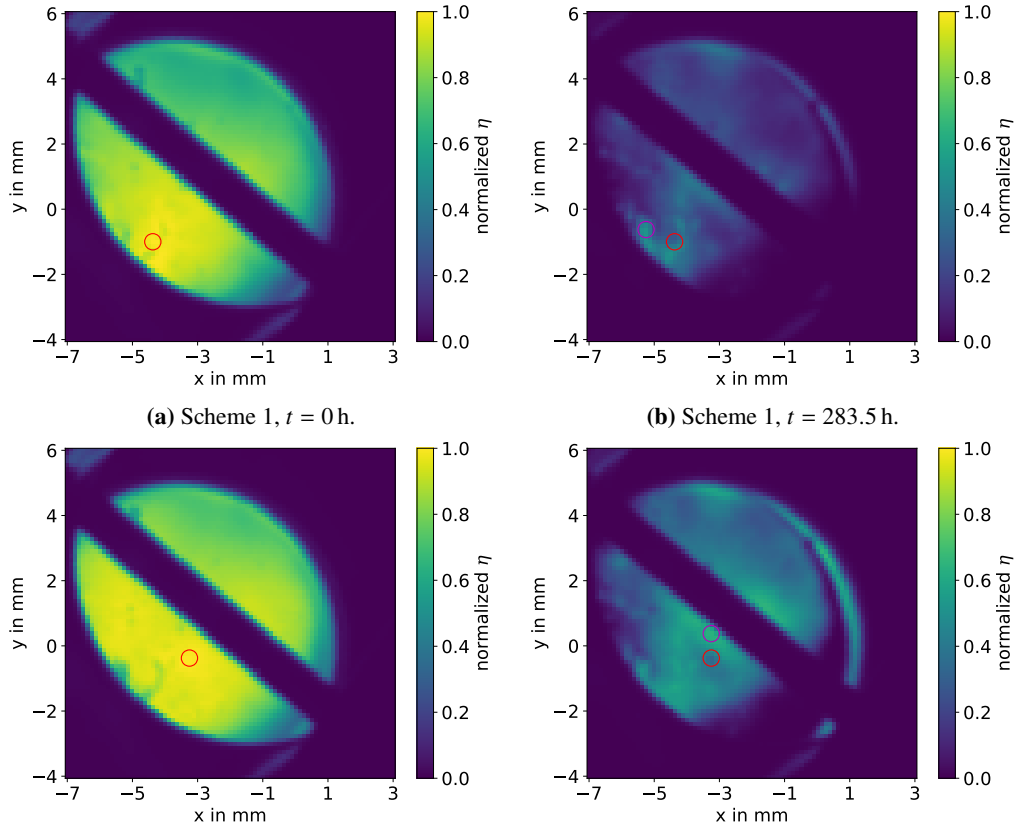

(a) Scheme 1, $t = 0\,\mathrm{h}$.

(b) Scheme 1, $t = 283.5\,\mathrm{h}$.

(c) Scheme 2, $t = 0\,\mathrm{h}$.

(d) Scheme 2, $t = 422.4\,\mathrm{h}$.

Figure 5: Normalized quantum efficiency scans for $\lambda = (785 \pm 2)\,\mathrm{nm}$ of the sample activated with schemes 1 ((a) and (b)) and 2 ((c) and (d)), taken at different times during photocathode operation. Some parts of the sample surface are obscured by the insulator and the Li dispenser of the activation assembly. The position of the maximum quantum efficiency of the first and second scan, η_1 and η_2, are marked with a red and purple circle, respectively. All corresponding quantum efficiency values are given in Table 3. The diameter of the circles is 500 µm, corresponding to the $1/e^2$ diameter of the laser spot on the photocathode surface. Each scan was normalized to η_1, i.e. the maximum quantum efficiency determined by the first surface scan directly after activation at $t = 0\,\mathrm{h}$.

80 % of the initial value remaining.

Table 4: Relative change R of the quantum efficiencies η_1, η_2, and η_3 between the initial scan (scan 1) at $t_1 = 0$ and the subsequent scans at t_2 (scan 2) and t_3 (scan 3).

Scheme	Time	$R(\eta_1)$	$R(\eta_2)$	$R(\eta_3)$
1	t_2	0.29 ± 0.01	0.63 ± 0.03	-
2	t_2	0.34 ± 0.02	0.68 ± 0.04	-
3	t_2	0.48 ± 0.03	0.79 ± 0.04	0.76 ± 0.04
	t_3	0.28 ± 0.02	0.41 ± 0.03	0.50 ± 0.03

These results show that the addition of Li yields a significant increase in dark lifetime as well

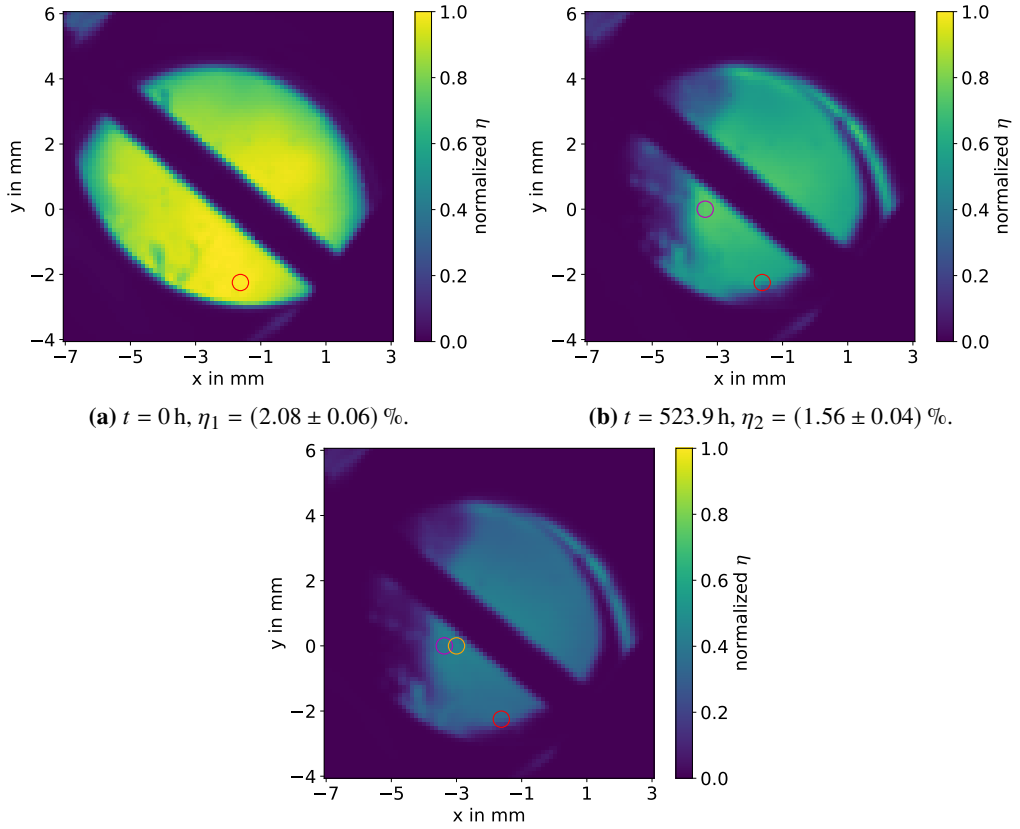

(a) $t = 0\,\mathrm{h}$, $\eta_1 = (2.08 \pm 0.06)$ %.

(b) $t = 523.9\,\mathrm{h}$, $\eta_2 = (1.56 \pm 0.04)$ %.

(c) $t = 742\,\mathrm{h}$, $\eta_3 = (1.00 \pm 0.03)$ %.

Figure 6: Normalized quantum efficiency scans for $\lambda = (785 \pm 2)$ nm of the sample activated with scheme 3, taken at different times during photocathode operation. The position of the maximum quantum efficiency of the first, second, and third scan, η_1, η_2, and η_3, are marked with a red, purple, and orange circle, respectively. All corresponding quantum efficiency values are given in Table 3. The diameter of the circles is 500 µm, corresponding to the $1/e^2$ diameter of the laser spot on the photocathode surface. Each scan was normalized to η_1, i.e. the maximum quantum efficiency determined by the first surface scan directly after activation at $t = 0\,\mathrm{h}$.

as in operational lifetime. The enhanced robustness of the layer in the regions where no beam is extracted offers the possibility to prolong the operational lifetime of the photocathode even further by moving the laser spot position. The scans conducted for scheme 3 also show the possible reason why the observed quantum efficiency trend fluctuated much more than those observed in other measurements. During the first run with the scheme-3 activated surface, the laser spot position was situated at the border between the center region and the bottom right corner of the photocathode, where the quantum efficiency decayed much faster than in the center. We assume that due to the failure of the air conditioning unit and subsequent changes in temperature within the laboratory, the laser spot position drifted between the two regions. This would explain the sudden changes in quantum efficiency visible in Figure 4 at around 140 h and 390 h. For future measurements, we plan to implement an on-line measurement and stabilization of the laser spot position.

6. Conclusion and Outlook

After extensive maintenance of the activation chamber, experiments with Cs-O_2 and Cs-O_2-Li activation procedures were conducted at Photo-CATCH. In addition to the previously established pulsed Li exposure during co-deposition of Cs and O_2, a new scheme featuring a continuous Li exposure was successfully tested. Both Li-enhanced activations showed a significant increase in both lifetime and extracted charge compared to standard Cs-O_2 activation. Surface scans revealed a higher stability of the surface layer in regions where no beam was extracted, enabling prolonged operational lifetime by means of changing the laser spot position.
The measurements in this work illustrate the challenge of identifying and controlling systematic variations capable of introducing changes in the observed quantum efficiency and lifetime parameters. This severely complicates the interpretation of cause and effect required to optimize the activation process, i.e. the quality of the NEA surface layer.

For future measurements, we aim to tackle this problem by implementing several measures such as dispenser input-power stabilization, online pressure control, and stabilization of the laser-spot position. Further measurements are planned to optimize the Cs-O_2-Li activation procedure, as well as investigating its effects on quantum efficiency, lifetime, and extracted charge.

References

[1] C.K. Sinclair, *DC photoemission electron guns as ERL sources*, *Nucl. Instrum. Methods, Sect. A* **557** (2006) .

[2] T. Rao et al., *Photocathodes for the energy recovery linacs*, *Nucl. Instrum. Methods, Sect. A* **557** (2006) .

[3] R. Heine, *Preaccelerator concepts for an energy-recovering superconducting accelerator*, *Phys. Rev. Accel. Beams* **24** (2021) 011602.

[4] F. Schliessmann, M. Arnold, L. Juergensen, N. Pietralla, M. Dutine, M. Fischer et al., *Realization of a multi-turn energy recovery accelerator*, *Nature Physics* (2023) .

[5] PEPPo Collaboration collaboration, *Production of highly polarized positrons using polarized electrons at MeV energies*, *Phys. Rev. Lett.* **116** (2016) 214801.

[6] L.S. Cardman, *The PEPPo method for polarized positrons and PEPPo II*, *AIP Conf. Proc.* **1970** (2018) 050001.

[7] A. Brachmann, J.E. Clendenin, E.L. Garwin, K. Ioakeimidi, R.E. Kirby, T. Maruyama et al., *The polarized electron source for the international collider (ILC) project*, *AIP Conf. Proc.* **915** (2007) 1091.

[8] G. Moortgat-Pick et al., *Polarized positrons and electrons at the linear collider*, *Physics Reports* **460** (2008) 131.

[9] J. Skaritka, E. Wang, F. Willeke, R. Lambiase, W. Lui, V. Ptitsyn et al., *Conceptual design of a Polarized Electron Ion Collider at Brookhaven National Laboratory*, *Proc. 17th International Workshop on Polarized Sources, Targets & Polarimetry — PoS(PSTP2017)*, vol. 324, 2018, 015.

[10] J. Kessler, *Polarized electrons*, Springer Berlin Heidelberg (1985), 10.1007/978-3-662-02434-8.

[11] N. Kurichiyanil, *Design and construction of a test stand for photocathode research and experiments*, doctoral dissertation, Technische Universität Darmstadt, Darmstadt, Juli, 2017. http://tuprints.ulb.tu-darmstadt.de/5903/.

[12] M. Herbert et al., *Inverted geometry photo-electron gun research and development at TU Darmstadt*, *Proc. 9th International Particle Accelerator Conference (IPAC'18)*, no. 9 in International Particle Accelerator Conference, JACoW Publishing, June, 2018, 4545.

[13] N. Pietralla, *The institute of nuclear physics at the tu darmstadt*, *Nuclear Physics News* **28** (2018) 4.

[14] N. Kurichiyanil, J. Enders, Y. Fritzsche and M. Wagner, *A test system for optimizing quantum efficiency and dark lifetime of GaAs photocathodes*, *J. Instrum.* **14** (2019) P08025.

[15] M. Herbert, *Electron emission from GaAs photocathodes using conventional and Li-enhanced activation procedures*, doctoral dissertation, Technische Universität Darmstadt, Darmstadt, 2022. http://tuprints.ulb.tu-darmstadt.de/20707/.

[16] M. Herbert, T. Eggert, J. Enders, M. Engart, Y. Fritzsche and V. Wende, *Automated Activation Procedure for GaAs Photocathodes at Photo-CATCH*, *Proc. 19th Workshop on Polarized Sources, Targets and Polarimetry — PoS(PSTP2022)*, vol. 433, 2023, 003.

[17] M. Herbert, *Negative electron-affinity activation procedures for GaAs photocathodes at Photo-CATCH*, *Proc. 14th International Particle Accelerator Conference (IPAC'23)*, no. 14 in IPAC'23 - 14th International Particle Accelerator Conference, JACoW Publishing, Geneva, Switzerland, 05, 2023, 1397.

[18] M. Herbert, T. Eggert, J. Enders, M. Engart, Y. Fritzsche, M. Meier et al., *Cs-O_2-Li as enhanced NEA surface layer with increased lifetime for GaAs photocathodes*, *Phys. Rev. Accel. Beams* **28** (2025) 013401.

[19] D.T. Pierce and F. Meier, *Photoemission of spin-polarized electrons from GaAs*, *Phys. Rev. B* **13** (1976) 5484.

[20] H. Sonnenberg, *Long-wavelength photoemission from InAs1-xPx*, *Applied Physics Letters* **19** (1971) 431.

[21] K.L. Jensen, D.W. Feldman, N.A. Moody and P.G. O'Shea, *A photoemission model for low work function coated metal surfaces and its experimental validation*, *J. Appl. Phys.* **99** (2006) 124905.

[22] J.J. Uebbing, *Use of auger electron spectroscopy in determining the effect of carbon and other surface contaminants on GaAs–Cs–O photocathodes*, *J. Appl. Phys.* **41** (1970) 802.

[23] T. Siggins, C. Sinclair, C. Bohn, D. Bullard, D. Douglas, A. Grippo et al., *Performance of a DC GaAs photocathode gun for the Jefferson lab FEL*, *Nucl. Instrum. Methods, Sect. A* **475** (2001) 549 FEL2000: Proc. 22nd Int. Free Electron Laser Conference and 7th F EL Users Workshop.

[24] F. Ciccacci and G. Chiaia, *Comparative study of the preparation of negative electron affinity GaAs photocathodes with O2 and with NF3*, *J. Vac. Sci. Technol. A* **9** (1991) 2991.

[25] B. Dunham et al., *Record high-average current from a high-brightness photoinjector*, *Appl. Phys. Lett.* **102** (2013) 034105.

[26] K. Aulenbacher, V. Tioukine, M. Wiessner and K. Winkler, *Status of the polarized source at MAMI*, *AIP Conf. Proc.* **675** (2003) 1088.

[27] G.A. Mulhollan and J.C. Bierman, *Enhanced chemical immunity for negative electron affinity GaAs photoemitters*, *J. Vac. Sci. Technol. A* **26** (2008) 1195.

[28] L. Cultrera, A. Galdi, J.K. Bae, F. Ikponmwen, J. Maxson and I. Bazarov, *Long lifetime polarized electron beam production from negative electron affinity GaAs activated with Sb-Cs-O: Trade-offs between efficiency, spin polarization, and lifetime*, *Phys. Rev. Accel. Beams* **23** (2020) 023401.

[29] G.A. Mulhollan, *Activation layer stabilization of high polarization photocathodes in sub-optimal rf gun environments*, *Scripta Metallurgica et Materialia* (2010) .

[30] M. Herbert, J. Enders, M. Poelker and C. Hernandez-Garcia, *Lifetime Measurements of GaAs photocathodes at the Upgraded Injector Test Facility at Jefferson Lab*, *Proc. 18th Workshop on Polarized Sources, Targets and Polarimetry — PoS(PSTP2019)*, vol. 379, 2020, 042.

PoS(PSTP2024)055